Journal of Nuclear Materials 399 (2010) 231–235

Contents lists available at ScienceDirect

Journal of Nuclear Materials

journal homepage: www.elsevier.com/locate/jnucmat

Corrosion of alumina-forming austenitic steel Fe–20Ni–14Cr–3Al–0.6Nb–0.1Ti in supercritical water

S.H. Nie *, Y. Chen, X. Ren, K. Sridharan, T.R. Allen

Department of Engineering Physics, University of Wisconsin, 1500 Engineering Dr., Madison, WI 53706, USA

ARTICLE INFO

Article history:
Received 30 October 2009
Accepted 25 January 2010

ABSTRACT

The oxidation behavior of alumina-forming austenitic (AFA) steel Fe–20Ni–14Cr–3Al–0.6Nb–0.1Ti has been examined after exposure to supercritical water (SCW) at 500 °C and 25 MPa pressure and with a dissolved oxygen content of 25 wppb, for exposure periods of 1300 h, 1700 h and 3000 h. A double layer oxide structure developed on all samples, consisting specifically of a Fe-rich outer hematite layer and an inner layer of Al–Cr–Fe-rich oxide containing a small fraction of FCC Ni-rich metal. Additionally, a thin Ni-rich layer in the bulk alloy close to the oxide/metal interface was also observed. Based on weight gain measurements, the oxidation resistance of the AFA steel was superior to other austenitic alloys, 800H, D9, and 316 stainless steel, tested under similar conditions. The formation of the protective Al–Cr–Fe-rich oxide layer may provide good long-term protection against corrosion in SCW environment.

1. Introduction

The supercritical water reactor (SCWR) has been selected as one of the reactor concepts for future Generation IV nuclear reactor systems, because of its simplified design, smaller volume, and higher thermal efficiency than current light water reactors (LWRs) [1]. However, supercritical water (water above the thermodynamic critical point, 374.2 °C temperature and 22.1 MPa pressure) is very corrosive to structural materials that would be used in the SCWR. Therefore, the corrosion behavior of candidate materials for the SCWR has to be thoroughly investigated prior to its safe application. Austenitic steels, ferritic–martensitic (F/M) steels and nickel-based alloys are being considered as candidates for future SCWR systems [2].

The key to good corrosion resistance is to establish a continuous layer of a slow-growing, thermodynamically stable oxide layer such that subsequent oxidation is limited by diffusion of metal or oxygen species across this layer. Cr_2O_3 and Al_2O_3 are the principal oxides that are responsible for the protection of metallic alloys in high-temperature applications. Al_2O_3 scales offer a superior protection compared to Cr_2O_3 in many high-temperature environments and in the presence of both oxygen and water vapor [3–11]. However, all cast and wrought iron-based, heat-resistant structural alloys utilize Cr_2O_3-based scales for protection [3–5]. This is due to the extensive solid solubility and excellent metallurgical compatibility of chromium in the Fe/(Fe, Ni) system for alloy design flexibility which allows for the optimization of oxidation and creep resistance. Ferritic Fe–Cr–Al-based alloys are capable of Al_2O_3 formation, but they have poor creep resistance resulting from their open body-centered cubic structure. Oxide dispersion strengthened (ODS) ferritic Fe–Cr–Al-based alloys [12] can form alumina scale and provide excellent high-temperature creep resistance, but high cost and large scale commercialization issues have thus far limited their use. To obtain Fe–Cr–Al-based alloys with creep resistance, an austenitic face-centered cubic structure is needed. A major complication for developing a successful AFA steel is that aluminum is a ferrite stabilizer. Furthermore, the alloys also require the addition of significant quantities of chromium, a ferrite stabilizer, to help promote protective Al_2O_3 scale formation. The desired austenitic matrix structure can be stabilized in these alloys by large additions of nickel which significantly increases the cost of these alloys.

Recently, Oak Ridge National Laboratory (ORNL) [13–19] initiated a program to develop creep-resistant AFA stainless steels with low levels of nickel, comparable to existing advanced austenitic stainless steels. High-temperature ultrafine-precipitation-strengthened (HT UPS) family of austenitic stainless steel alloys [20] was used as a starting point for alloy modification. The findings of this study to date indicate that increasing niobium, aluminum, and/or nickel content favor the establishment and maintenance of a stable protective Al_2O_3 layer [16,18], although the mechanisms underlying these trends are not fully understood. AFA alloys show a promising combination of oxidation resistance, creep resistance, tensile properties, and potential for good welding behavior. The optimum alloy composition that emerged from this study was in the range of Fe–(20–25)Ni–(12–15)Cr–(3–4)Al–(1–3)Nb wt.% base.

The work described in this paper investigates the corrosion performance of first generation AFA alloy Fe–20Ni–14Cr–3Al–0.6Nb–

* Corresponding author. Tel.: +1 608 263 6371; fax: +1 608 263 7451.
E-mail address: snie2@wisc.edu (S.H. Nie).

0022-3115/$ - see front matter © 2010 Elsevier B.V. All rights reserved.
doi:10.1016/j.jnucmat.2010.01.025

0.1Ti [18] exposed to SCW with 25 wppb dissolved oxygen content at 500 °C, 25 MPa pressure for exposure periods of 1300 h, 1700 h and 3000 h. The alloy was prepared on an experimental, laboratory scale level to determine the feasibility of producing larger scale castings with similar properties.

2. Experimental

The AFA (Fe–20Ni–14Cr–3Al–0.6Nb–0.1Ti wt.%) alloy for this study in the as-received was solution heat treated at 1250 °C for 2 h, cold worked 50%, and then recrystallized at 1200 °C for 30 min, and had an average grain size of 35.7 μm. The as-received bulk AFA was cut into coupons of dimension 31.75 mm × 12.7 mm × 0.34 − 0.49 mm, and samples for SCW testing were progressively ground and polished concluding with a final polishing step with a 1 μm diamond paste.

All SCW exposure tests were performed at a temperature of 500 °C at a pressure of 25 MPa with a flow rate of about 1 m/s, and a 25 wppb dissolved oxygen content at the test section inlet. To study the effects of exposure time in SCW on the corrosion behavior of alloys, the separate samples were pulled out and analyzed after exposure times of 1300 h, 1700 h and 3000 h, respectively.

All the samples were weighed before and after the corrosion tests using a SCIENTECH SA-80 Milligram Balance with an accuracy of 0.1 mg to monitor the weight change due to oxidation. To minimize the random measurement error, every measurement was repeated four times, and the arithmetical average value is reported. A JEOL JSM-6100 scanning electron microscope (SEM), equipped with an energy dispersive X-ray spectroscopy (EDS), was used to investigate the oxide morphology, chemical composition and oxide thickness. Phase identification was performed using STOE X-ray (Cu Kα radiation, $\lambda = 1.54060$ Å) diffraction (XRD) and a Thermo-Fisher Scientific K-Alpha X-ray Photoelectron Spectroscopy system. XPS analysis was performed after sputtering to a depth of 500 nm using Ar^+ at 3 keV. The depth was based on pre-determined sputter rate of 0.2 nm/s determined using a tantalum-pentoxide standard.

3. Results and discussion

The surface morphology of the oxide layer formed on the samples after various exposure times in SCW is shown in Fig. 1. A polycrystalline oxide structure is observed with the size and number of oxide grains increasing with exposure time, and the interspacing between the grains decreasing with exposure time. These interspacings would act as pathways for the transport of oxygen or metal ions [21]. Contrasting the three exposures, groups of loose oxide grains only grow on certain parts of the surface of the sample with 1300 h exposure; while for the 1700 h and 3000 h exposures, the oxide grains cover the entire surface. The formation of this oxide is due to the diffusion of iron from the bulk alloy, driven by the high chemical potential of oxygen at the SCW/oxide interface [13]. There was no oxide exfoliation observed for any of the tested samples.

Fig. 2 shows the SEM images of the cross-section of the oxide layers that formed on samples exposed for various exposure times. The corresponding cross-sectional chemical composition profiles of the oxide layer for the 1700 h exposure is shown in Fig. 3. The XPS elemental spectra of oxide at a location reached after a 500 nm sputtering from the surface are shown in Fig. 4. Based on the morphology, elemental cross-sectional concentration distribution and XPS elemental analysis results, the oxide scale formed at all three exposure times can be classified into two distinct layers, a Fe-rich outer oxide layer and an inner Al–Cr–Fe-rich oxide layer. This inner Al–Cr–Fe-rich oxide layer also contained FCC Ni-rich metal, which has been confirmed by TEM composition and diffraction pattern analysis. The thickness of the oxide layer increased with the exposure time, and the total thickness of the oxide layers were about 1 μm, 2.5 μm, and 3.5 μm, for the 1300 h, 1700 h, and 3000 h exposures, respectively. Additionally, a thin Ni-rich layer in the bulk alloy close to the oxide/metal interface was also observed by SEM-EDS sectional analysis as shown in Figs. 2 and 3. This layer is incorporated in the diffusion or internal oxidation layer, where the chemical composition varied gradually from oxide to bulk alloy concentration.

The distribution of various elements in the oxide layer can be attributed to their differing affinities for oxygen [22]. For example, since the oxygen affinity for Al and Cr is larger than that of Fe, they will oxidize more readily by reacting with diffused oxygen to form an Al–Cr-rich inner oxide layer. Fe can diffuse outward and react with oxygen at the interface of the oxide/SCW to form a Fe-rich outer oxide layer. Finally Ni will be concentrated at the interface between the oxide and metal because Ni is the least likely to be oxidized in AFA Fe–20Ni–14Cr–3Al–0.6Nb–0.1Ti. This is also the reason why some FCC Ni-rich phases were left in the Al–Cr–Fe-rich oxide layer. Simultaneously, the formation of the oxide layer will lower the oxygen potential at the oxide/metal interface making iron oxides less stable [23]. With the growth of this layer, it should also decrease the diffusion rate and subsequently hamper further development of scale, acting as a barrier against the diffusion of metal and oxygen ions [24]. Oxidation is subsequently governed by this slow-growing, inner Al–Cr–Fe-rich oxide layer. These are the key reasons for the high corrosion resistance resulting from aluminum and chromium additions to iron-based alloys under these conditions.

In addition, some porosity is observed at the interface between the two oxide layers. These pores become finer in size and less frequent with exposure time. The pores likely evolve in the initial stages of oxide nucleation. Subsequently, initial grains grow larger by the reaction between dissolved oxygen and iron ions that diffuse from the bulk alloy, and as the grains grow, the pore size decreases.

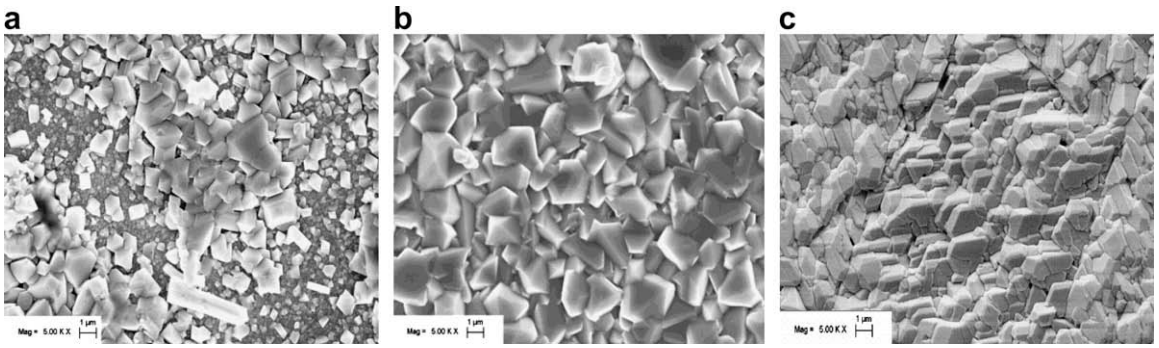

Fig. 1. Surface morphology of the oxide layer on the samples after SCW exposure for various times (a) 1300 h, (b) 1700 h and (c) 3000 h.

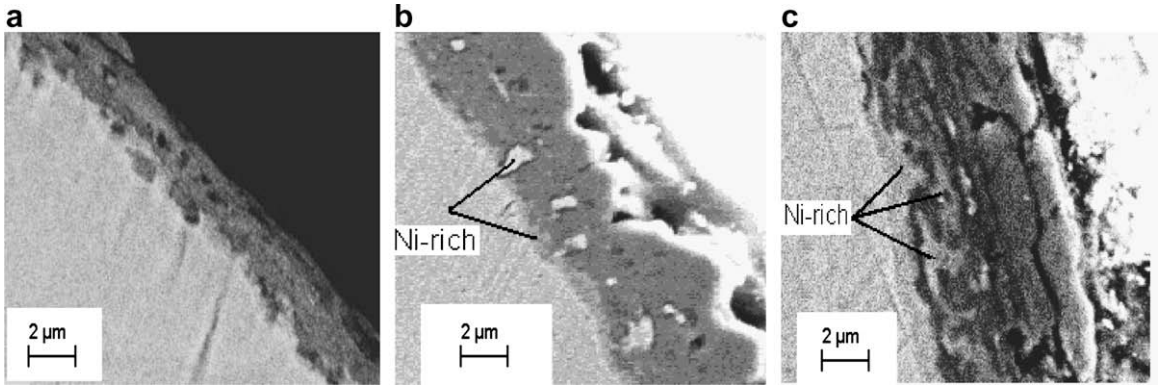

Fig. 2. SEM images of the cross-section of the oxide layers formed on the (AFA) Fe–20Ni–14Cr–3Al–0.6Nb samples after exposure to SCW for various exposure times. (a) 1300 h, (b) 1700 h and (c) 3000 h.

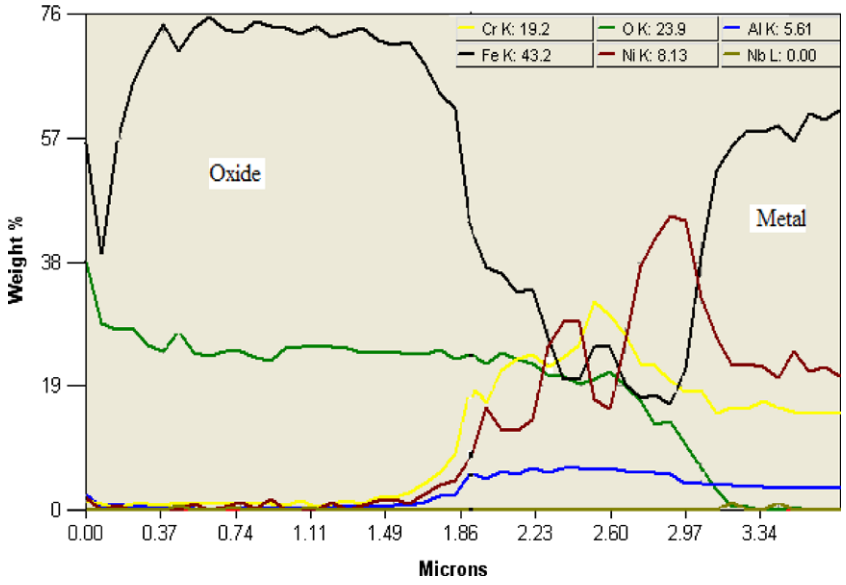

Fig. 3. Elemental depth profiles, as measured using the EDS capability of the JEOL SEM, of (AFA) Fe–20Ni–14Cr–3Al–0.6Nb sample exposed to 25 wppb dissolved oxygen content SCW at 500 °C for 1700 h.

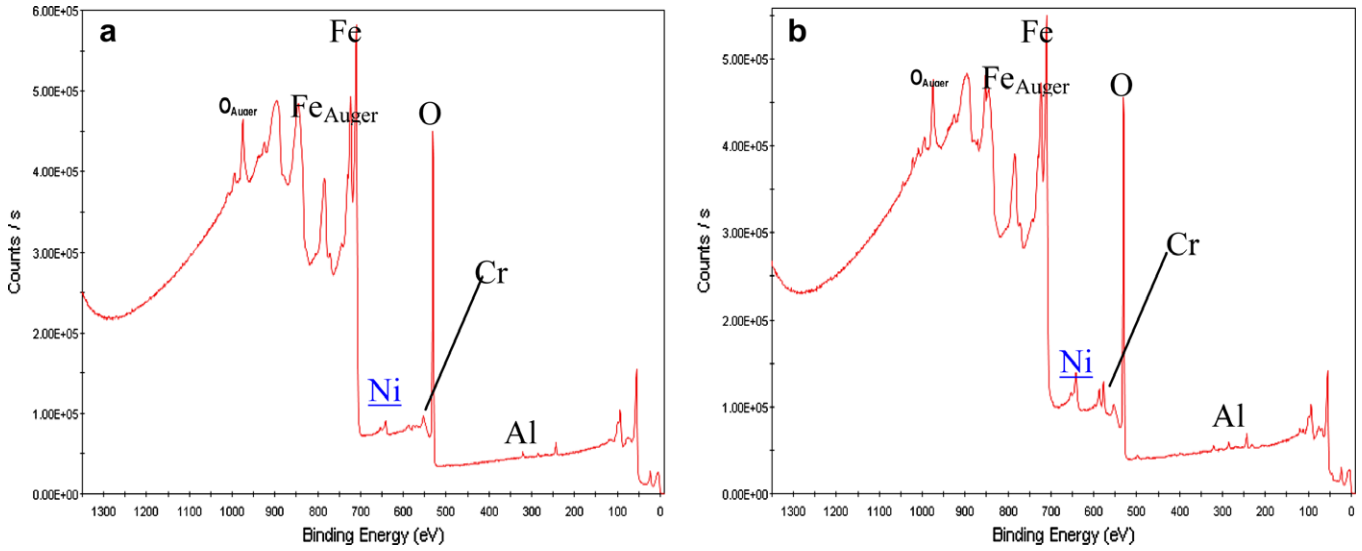

Fig. 4. XPS elemental analysis spectrum of (AFA) Fe–20Ni–14Cr–3Al–0.6Nb samples after SCW different exposure to varying times at a 500 nm etch cross-section depth (a) 1300 h and (b) 3000 h.

The results from XPS in Fig. 4 show that the elements in 500 nm oxide layer depth are iron (36.56% atom) and oxygen (61.58% atom), and a very little Ni, Al and Cr is observed. This result further indicates that the oxide from the outer surface to at least a depth of 500 nm could be mainly hematite. This result is consistent with that in Figs. 3 and 5.

The phase structures of oxides formed on the samples exposed to SCW for different exposure times were confirmed by XRD spectra shown in Fig. 5. In the spectra for the sample exposed for 1300 h in SCW, austenite is the primary phase; for the 1700 h exposure, three phases namely austenite, hematite and Fe–Cr–Al oxide were observed; for the 3000 h exposure, hematite and spinel were the two main phases with only a marginal signal from the austenite phase. The austenite signal gradually disappears because the oxide layer becomes thicker.

Fig. 6 shows the limited weight gain data of AFA Fe–20Ni–14Cr–3Al–0.6Nb–0.1Ti, compared with austenitic alloys 800H and D9 and austenitic stainless steel 316, which were tested under similar conditions. It was observed that AFA Fe–20Ni–14Cr–3Al–0.6Nb–0.1Ti has a lower overall weight gain compared with SS316, 800H and D9 during the 3000 h testing time. The experimental weight gain (WG) data can be fitted using the following equations:

$$WG = kt^n \quad (1)$$

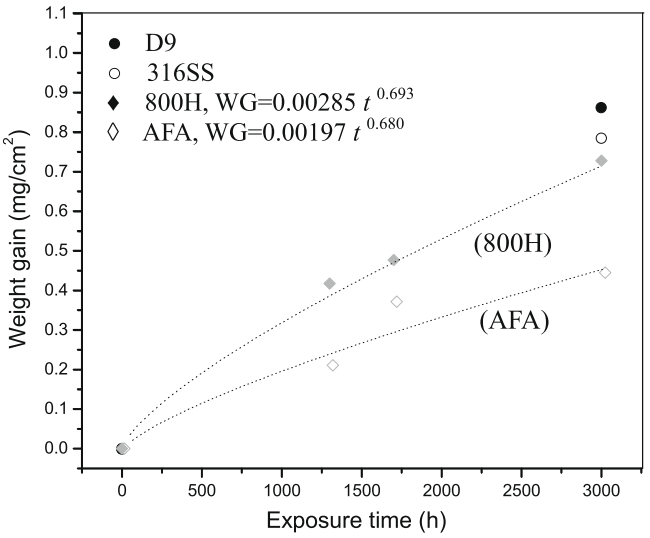

Fig. 6. The weight gain of AFA Fe–20Ni–14Cr–3Al–0.6Nb–0.1Ti exposed to SCW for 1300 h, 1700 h and 3000 h, respectively at 500 °C, 25 MPa and 25 wppb oxygen content.

where WG is weight gain, t is the exposure time, k is a constant, and n is the time exponent. Fig. 6 shows the weight gain for the AFA

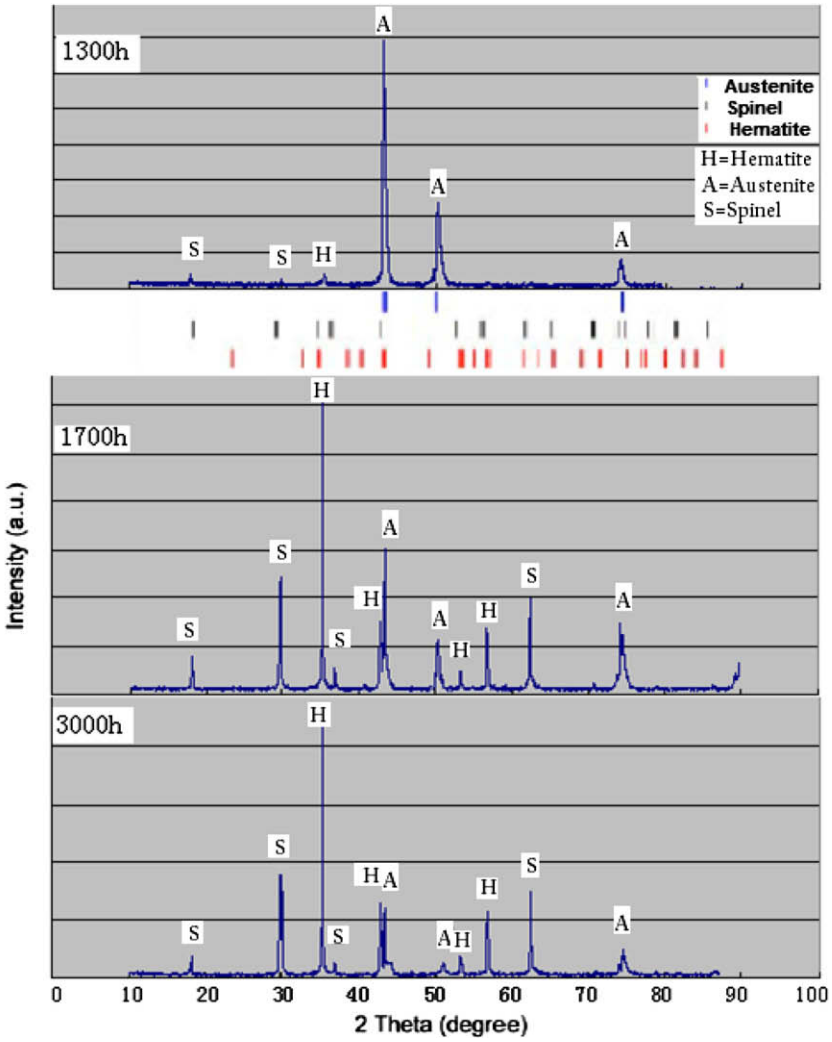

Fig. 5. X-ray diffraction patterns of (AFA) Fe–20Ni–14Cr–3Al–0.6Nb samples exposed to 25 wppb dissolved oxygen content SCW at 500 °C for 1300 h, 1700 h and 3000 h.

steel and other alloys plotted using the above model. The time exponents are 0.680 and 0.693, respectively for AFA, and 800H. The results also show AFA should have smallest weight gain trends for longer exposure time; the k constants are 0.00197 and 0.00285, respectively for AFA, and 800H. The superior oxidation resistance is likely due to the formation of the Al–Cr–Fe-rich oxide layer in the AFA steels.

4. Conclusion

The oxidation behavior of a relatively new alumina-forming austenite (AFA) alloy (Fe–20Ni–14Cr–3Al–0.6Nb–0.1Ti) in supercritical water containing 25 wppb oxygen at 500 °C for 1300 h, 1700 h, and 3000 h, has been investigated. The oxide scale formed on the alloy after all three exposures consisted of an outer hematite layer and an inner layer with Al–Cr–Fe–spinel oxide containing FCC Ni-rich intermetallic compounds. A Ni-rich thin layer in the bulk alloy close to the oxide/metal interface was also observed. Based on weight gain measurements, the AFA steel exhibited a superior corrosion resistance compared to austenitic alloys 316SS, 800H and D9, tested under same conditions. This improved performance of the AFA alloy stems from the formation of a protective Al–Cr–Fe-rich oxide layer on the surface of this alloy.

Acknowledgements

The authors are grateful to Drs. Mark Anderson, Jeremy Licht, and Lizhen Tan for SCW tests and Roger Staehle for helpful discussion. This work is supported by the Idaho National Engineering and Environmental Laboratory as part of the Department of Energy Generation IV Initiative and by the Department of Energy, Office of Nuclear Energy, Science, and Technology as part of INERI grants 2003–2008-K. This research utilized NSF-supported shared facilities at the University of Wisconsin. The authors also thank Dr. Michael Brady of Oak Ridge National Laboratory for providing the AFA material for analysis. The authors are grateful to Dr. Jon McCarthy of University of Wisconsin Materials Science Center and Dr. Paul Mack of Thermo Fisher Scientific for their assistance in the XPS analysis.

References

[1] A Technology Roadmap for Generation IV Nuclear Energy Systems. US DEO Nuclear Energy Research Advisory Committee and the Generation IV International Forum, December 2002.
[2] T.R. Allen, Workshop on Higher Temperature Materials for Advanced Nuclear Energy Systems, DOE Office of Nuclear Energy, Science and Technology, La Jolla, CA, March 18, 2002.
[3] Alloys, ASM International, Materials Park, OH, 1990.
[4] B. Gleeson, Corrosion and Environmental Degradation, in: M. Schutze (Ed.), Materials Science and Technology Series, vol. 2, Wiley-VCH, Weinheim, Germany, 2000, pp. 173–228 (Chapter 5).
[5] P. Kofstad (Ed.), High Temperature Corrosion, Elsevier, London, 1988.
[6] M.P. Brady, B. Gleeson, I.G. Wright, JOM 52 (1) (2000) 16–21.
[7] J. Doychak, in: J.H. Westbrook, R.L. Fleischer (Eds.), Intermetallic Compounds: Principles and Practice, vol. 1, New York, John Wiley & Sons, 1994, pp. 977–1016.
[8] G.H. Meier, Mater. Corros. 47 (11) (1996) 595–618.
[9] G. Welsch et al., in: G. Welsch, P.D. Desai (Eds.), Oxidation and Corrosion of Intermetallic Alloys, Purdue Research Foundation, West Lafayette, IN, 1996, pp. 121–266.
[10] G.J. Yurek, in: F. Mansfeld (Ed.), Corrosion Mechanisms, Marcel Dekker, Inc., New York, 1987, pp. 398–446.
[11] E.J. Opila, Mater. Sci. Forum 461–464 (2004) 765–773.
[12] F.G. Wilson, B.R. Knott, C.D. Desforges, Met. Mater. Trans. A 9 (2) (1978) 275–282.
[13] M.P. Brady, Y. Yamamoto, M.L. Santella, P.J. Maziasz, B.A. Pint, C.T. Liu, JOM 60 (7) (2008) 12–18.
[14] Y. Yamamoto et al., Science 316 (5823) (2007) 433–436.
[15] Y. Yamamoto et al., Metall. Mater. Trans. A 38A (11) (2007) 2737–2746.
[16] M.P. Brady et al., Scripta Mater. 57 (12) (2007) 1117–1120.
[17] Y. Yamamoto et al., Intermetallics 16 (3) (2008) 453–462.
[18] M.P. Brady, Y. Yamamoto, M.L. Santella, L.R. Walker, Oxid. Met. 72 (5–6 December) (2009) 311–333.
[19] Y. Yamamoto, M.L. Santella, M.P. Brady, H. Bei, P.J. Maziasz, Metall. Mater. Trans. A. 40 (8) (2009) 1868.
[20] P.J. Maziasz, JOM 41 (7) (1989) 14–20.
[21] A. Atkinson, Rev. Mod. Phys. 57 (1985) 437.
[22] G.E. Totten, M.A.H. Howes, Steel Heat Treatment Handbook, Marcel Dekker, New York, 1997.
[23] M. Ueda, M. Nanko, K. Kawamura, T. Maruyama, Mater. High Temp. 20 (2003) 109.
[24] R. Hales, Mater. Corros. 29 (1978) 393.